https://doi.org/10.3311/PPch.45185
Creative Commons Attribution

Periodica Polytechnica Chemical Engineering

Thickness-Dependent Non-Ideal Behavior of Copolymer Solar Cells: A Numerical Investigation in Density Functional Theory and Solar Cell Capacitance Simulator Frameworks

Anthony C. Ozurumba[1], Vincent N. Okechukwu[1], Musa I. Salami[2], Eli Danladi[3,4*], Bunmi J. Akeredolu[5,6], Madan M. Gururani[7], Salisu I. Kunya[8], Esther O. Ngbede[9,10], Inalegwu A. Ngbede[4,11], Robinson Musembi[12], Kuvondik Dovranov[13], Muhammed O. Abdulmalik[12,14], Daniel Thomas[15], Abdulrazak Zubairu[15], Nicholas N. Tasie[16], Emmanuel Igumbor[17], Bala I. Adamu[15], Mokhotjwa S. Dhlamini[15], Lehlohonolo F. Koao[5], Tshwafo E. Motaung[18], Setumo V. Motloung[19]

[1] Africa Center of Excellence in Future Energies and Electrochemical Systems, Federal University of Technology, Owerri, Nigeria
[2] Department of Physics and Engineering Physics, Morgan State University, 1700 East Cold Spring Lane, Baltimore, MD, USA
[3] Department of Mathematical and Physical Sciences, Central University of Technology, Free State, South Africa
[4] Department of Physics, Federal University of Health Sciences, Otukpo, Benue State, Nigeria
[5] Department of Physics, Federal University Wukari. Taraba State, Nigeria
[6] Department of Physics, University of the Free State (Qwaqwa Campus), Private Bag X 13, Phuthaditjhaba, 9866, South Africa
[7] Department of Physics, M.B. Government P.G. College, Haldwani (Uttarakhand), India
[8] Department of Applied Physics, Federal University of Technology, Babura, Jigawa State, Nigeria
[9] Department of Chemistry, Federal University of Santa Maria, Brazil
[10] Department of Chemistry Education, Federal College of Education (Technical), Asaba, Delta State, Nigeria
[11] Department of Physics, Federal University of Santa Maria, Brazil
[12] Department of Physics, University of Nairobi, P.O.B. 30197-00100, Nairobi, Kenya
[13] Department of Physics, Karshi State University, 180119, Karshi, Uzbekistan
[14] Department of Physics, Confluence University of Science and Technology, Osara, Kogi State, Nigeria
[15] Department of Physics, College of Science, Engineering and Technology, University of South Africa, Johannesburg 1710, South Africa
[16] Department of Physics, Rivers State University, Port Harcourt, Rivers State, Nigeria
[17] Department of Mechanical Engineering Science, University of Johannesburg, Auckland Park, Johannesburg, South Africa
[18] Department of Chemistry and Chemical Technology, Sefako Makgatho Health Science University, P.O.B. 94, Medunsa, 0204, South Africa
[19] Directorate: Postgraduate Studies, Central University of Technology, Private Bag X 20539, Bloemfontein, 9300, South Africa
* Corresponding author, e-mail: danladielibako@gmail.com

Received: 17 June 2026, Accepted: 28 August 2026, Published online: 26 November 2026

Abstract

Organic photovoltaics based on poly(p-phenylene vinylene) derivatives offer compelling advantages for decentralized energy generation in tropical regions, yet their thickness-dependent performance limitations remain poorly understood. Herein, we present a comprehensive multiscale investigation of inverted FTO/TiO_2/BEHP-*co*-MEH-PPV/PEDOT:PSS/Au solar cells, combining density functional theory (DFT) with device-level solar cell capacitance simulator in 1-dimension SCAPS-1D, where fluorine-doped tin oxide (FTO) is a transparent conductive electrode, BEHP-*co*-MEH-PPV (poly{[2-[2',5'-bis(2"-ethylhexyloxy)phenyl]-1,4-phenylenevinylene]-*co*-[2-methoxy-5-(2'-ethylhexyloxy)-1,4-phenylenevinylene]}) is a poly(phenylenevinylene) derivate that is highly resistant to photodegradation and used as an active layer in our study, and poly(3,4-ethylenedioxythiophene) polystyrene sulfonate (PEDOT:PSS) is a mixed electron-ion conducting polymer. DFT calculations reveal a fundamental bandgap of 1.45 eV with highly delocalized frontier orbitals, confirming strong visible-light harvesting capability. Device simulations demonstrate that increasing active layer thickness from 0.1 to 1.0 μm enhances short-circuit current density from 7.1 to 12.7 mA/cm^2 through improved photon absorption. However, this optical gain is counterbalanced by severe fill factor degradation (87% to 24%) and open-circuit voltage suppression, driven by Shockley-Read-Hall trap-assisted recombination and quadratic series resistance scaling. Under ideal conditions (negligible bulk defects), the copolymer achieves 13.7% power conversion efficiency at 1.0 μm thickness, whereas realistic conditions limit performance below 0.16%. These findings establish that while BEHP-PPV-*co*-MEH-PPV exhibits excellent intrinsic optoelectronic properties and environmental stability, reducing bulk trap states through interfacial passivation is essential to achieve the thickness-dependent efficiency performance required for scalable, high-performance organic photovoltaics.

Keywords

organic photovoltaics, BEHP-*co*-MEH-PPV, DFT, SCAPS-1D, thickness-dependent recombination

Cite this article as: Ozurumba, A. C., Okechukwu, V. N., Salami, M. I., Danladi, E., Akeredolu, B. J., Gururani, M. M., Kunya, S. I., Ngbede, E. O., Ngbede, I. A., Musembi, R., Dovranov, K., Abdulmalik, M. O., Thomas, D., Zubairu, A., Tasie, N. N., Igumbor, E., Adamu, B. I., Dhlamini, M. S., Koao, L. F., Motaung, T. E., Motloung, S. V. "Thickness-dependent Non-ideal Behavior of Copolymer Solar Cells: A Numerical Investigation in DFT and SCAPS-1D frameworks", Periodica Polytechnica Chemical Engineering, 2026. https://doi.org/10.3311/PPch.45185

1 Introduction

The transition toward sustainable, decentralized energy generation is a critical imperative for developing energy markets, where expansive grid infrastructure remains uneven, and the demand for localized, off-grid power solutions continues to accelerate. Organic photovoltaics (OPVs), particularly copolymer solar cells (CSCs), offer a compelling pathway for scalable energy harvesting due to their low manufacturing costs, mechanical flexibility, and amenability to solution-processing techniques. However, the deployment of CSCs in real-time conditions is frequently bottlenecked by the environmental instability of the active layer and intrinsic limitations in charge carrier mobility. Among the various conjugated polymers investigated, derivatives of poly(p-phenylene vinylene) (PPV) have historically played a foundational role in organic optoelectronics. Notably, the copolymer poly{[2-[2′,5′-bis(2″-ethylhexyloxy)phenyl]-1,4-phenylene vinylene]-*co*-[2-methoxy-5-(2′-ethylhexyloxy)-1,4-phenylene vinylene]}(BEHP-PPV)-*co*-(MEH-PPV) is a poly(phenylene vinylene) derivate, that is highly resistant to photodegradation and used as an active layer, has emerged as a material of significant interest. It is a highly soluble copolymer that is demonstrably more stable to the photooxidation process than other phenyl-substituted PPV derivatives [1]. This inherent robustness against photodegradation makes it a highly attractive candidate for deployment in regions characterized by intense solar irradiance and elevated ambient conditions, provided that the device architecture can effectively manage charge extraction without the need for stringent inert-atmosphere processing.

While previous experimental reports on BEHP-PPV-*co*-MEH-PPV have established its baseline photooxidative stability and demonstrated proof-of-concept devices with modest efficiencies [2–5], this study provides the first comprehensive, multiscale theoretical framework coupling density functional theory (DFT) with solar cell capacitance simulator in 1-dimension (SCAPS-1D) to decouple optical generation from electrical collection limits in this copolymer system. Specifically, we isolate the impact of thickness-dependent non-idealities (parasitic resistances, trap-assisted recombination, and thermal stress) that bottlenecks scalable, large-area manufacturing. This contributes directly to the design of future organic photovoltaics by establishing the critical thickness threshold. Optical gains are negated by transport losses, a vital metric for decentralized energy deployment in tropical regions, where manufacturing infrastructure may be resource-constrained.

Despite the favorable optoelectronic properties of BEHP-*co*-MEH-PPV, optimizing the power conversion efficiency of these devices requires navigating a fundamental trade-off between optical absorption and electrical charge collection. To maximize photon harvesting, an optically thick active layer is theoretically desirable. Conversely, the inherently low charge carrier mobilities and short exciton diffusion lengths characteristic of conjugated polymers dictate the use of ultra-thin active layers to prevent severe recombination losses [6]. In resource-constrained research and manufacturing environments, depositing uniform, defect-free ultra-thin films over large areas with cost effective infrastructure is highly challenging. When the active layer thickness is increased to accommodate scalable, large-area coating techniques, the device invariably exhibits thickness-dependent non-ideal behavior. The non-ideal behavior of the diode is heavily correlated with the film thickness, manifesting as increased series resistance, space-charge accumulation, and non-geminate recombination dynamics [7]. Consequently, understanding the interplay between the molecular electronic structure of the copolymer and the macroscopic device physics is imperative for engineering durable solar cells that balance manufacturing tolerances with electrical efficiency.

In this work, we present a comprehensive theoretical investigation into the thickness-dependent non-ideal behavior of inverted FTO/TiO_2/BEHP-*co*-MEH-PPV/PEDOT:PSS/Au solar cells, where FTO is a transparent conductive electrode and poly(3,4-ethylenedioxythiophene) polystyrene sulfonate (PEDOT:PSS) is a mixed electron-ion conducting polymer. We employ DFT calculations to elucidate the ground-state electronic properties, frontier molecular orbitals, and optical bandgap of the BEHP-*co*-MEH-PPV copolymer. Subsequently, these intrinsic parameters validate the parameters integrated into SCAPS-1D to model the macroscopic device performance. By varying the active layer thickness, we decouple the optical generation profile from the electrical collection efficiency, specifically analyzing the degradation of the fill factor and the progression of the diode ideality factor. This study, thus, aims to provide a rigorous theoretical framework for maximizing the performance of environmentally stable copolymer-based solar cells under realistic operational constraints.

2 Theoretical methodology

2.1 Device architecture

The simulated device adopted an n-i-p planar heterojunction architecture with the layer sequence FTO/TiO_2/BEHP-*co*-MEH-PPV/PEDOT:PSS/Au, where fluorine-doped tin oxide (FTO) served as the front transparent conducting electrode, TiO_2 as the n-type electron transport layer (ETL), BEHP-*co*-MEH-PPV as the light-absorber layer, PEDOT:PSS as the hole transport layer (HTL), and Au as the back contact interfacial layer (see Fig. 1). Each layer was assigned thickness, bandgap, electron affinity, dielectric permittivity, effective density of states, carrier mobility, and doping concentration, drawn from published experimental and simulation studies [4, 5]. The TiO_2/BEHP-*co*-MEH-PPV and BEHP-*co*-MEH-PPV/PEDOT:PSS interfaces were modelled with a neutral defect level of total density (10^{10}/cm^2) using single-energy trap distributions.

2.2 Density functional theory calculations for the light absorber layer

First-principles density functional theory calculations of BEHP-*co*-MEH-PPV were performed using the DMol^3 module as implemented in the BIOVIA Materials Studio software package [8]. The exchange-correlation energy was described by the Perdew–Burke–Ernzerhof (PBE) functional within the generalised gradient approximation (GGA), striking a practical balance between computational efficiency and accuracy for the prediction of electronic structures [9]. Given the conjugated nature of the BEHP-*co*-MEH-PPV backbone, where intermolecular interactions and chain stacking play a critical role, Grimme's DFT-D dispersion correction was explicitly enabled to account for weak van der Waals forces often neglected by standard GGA functionals [10]. The double numerical plus polarisation (DNP) basis set, which is comparable in quality to Gaussian 6-31G** basis sets, was employed. DNP yields accuracy comparable to much larger Gaussian basis sets while maintaining superior cost-effectiveness [11]. Spin-polarisation was treated within the restricted formalism, and the overall charge of the system was set to neutral. The self-consistent field (SCF) calculations were converged with a medium tolerance and fine orbital cutoff quality, utilizing a fine k-point mesh (1 × 1 × 1) appropriate for isolated molecular systems. The global orbital cutoff radius was set to 3.7 Å, which is sufficient to include all valence atomic orbitals. Integration was performed on a coarse real-space grid, which is well-suited for evaluating the auxiliary density in periodic geometries. Symmetry was disabled to allow full structural relaxation without imposed constraints.

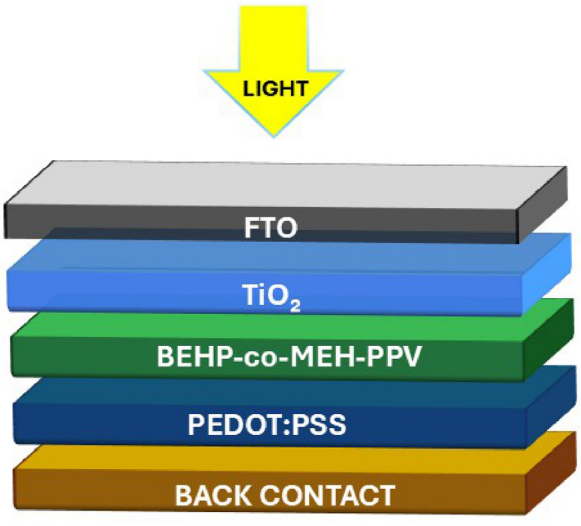

Fig. 1 Schematic illustration of the proposed solar cell

2.3 Solar cell capacitance simulator, 1-dimension calculation

The device simulation was carried out using the solar cell capacitance simulator in one dimension (SCAPS-1D, version 3.3.10), developed at the University of Gent, Belgium. SCAPS-1D software simulates solar cells by numerically solving the semiconductor equations that govern defects, recombination, and charge generation [12]. Known for its user-friendly interface, it accurately predicts key performance metrics like efficiency, fill factor, current, and voltage. The programme solves the Poisson equation and the continuity equations for electrons and holes under steady-state conditions,

$$\frac{d^2}{dx^2}\varphi(x)=\frac{e}{\varepsilon_0\varepsilon_r}\begin{pmatrix}p(x)-n(x)+N_D\\-N_A+\rho_{\text{defect}}\left(p(x),n(x)\right)\end{pmatrix}, \tag{1}$$

$$-\frac{1}{J}\frac{dJ_p}{dx}+R_p(x)-G(x)=0, \tag{2}$$

$$-\frac{1}{J}\frac{dJ_n}{dx}+R_n(x)-G(x)=0, \tag{3}$$

where the variables observed in the equations are potential of electrostatic (Ψ), electron charge (e), relative permittivity (ε_r, the measure of a substance's behavior in an electric field), permittivity of vacuum (ε_0), electron distribution (ρ_n), electron density (n), hole density (p), hole distribution (ρ_p), current densities of electrons (J_n), hole current densities (J_p), rate of recombination (R), x represents the spatial coordinate, and generation rate (G) [13, 14].

The device structure was defined sequentially from the front contact to the back contact, with each layer assigned material parameters drawn from published experimental and computational sources (see Tables 1–3) [15–19]. The simulations were performed under Air Mass 1.5 Global (AM1.5G, which indicates the thickness of atmosphere that sunlight must traverse) illumination (100 mW/cm^2) at 300 K. Ideal conditions were first established by setting bulk and interface defect densities to minimal values and neglecting parasitic resistances, optical losses, radiative recombination, and Auger recombination. Non-ideal conditions were then introduced individually: bulk defect densities, N_t (10^{15}/cm^3), series resistance, R_s (10 Ω·cm^2), shunt resistance, R_{sh} (10^2 Ω·cm^2), front-surface reflection losses (10%), radiative recombination coefficients (B) (3.125×10^{-10} cm^3/s), Auger recombination coefficients (C) (1.1221×10^{-28} cm^6/s), and working temperature (360 K) using literature-derived values [4]. These non-ideal parameters were systematically selected based on empirical literature for conjugated polymers, accurately reflecting the inherent bulk trap densities and parasitic resistances characteristic of scalable organic photovoltaics. This rigorous selection ensures that the SCAPS-1D simulations reliably model the practical performance limits of the inverted BEHP-*co*-MEH-PPV architecture under realistic operational constraints. The output parameters were extracted at each simulation step.

Table 1 Material parameters for ideal SCAPS-1D simulation

Parameters	FTO [15, 16]	TiO_2 [15, 16]	BEHP-*co*-MEH-PPV [4, 5]	PEDOT:PSS [17, 18]
Thickness (μm)	0.05	0.1	0.2	0.1
Bandgap, E_g (eV)	3.5	3.2	2.12	1.8
Electron affinity, χ (eV)	4	3.9	3.9	3.4
Relative dielectric permittivity, ε_r	9	9	30	3
Electron mobility, μ_e (cm^2/Vs)	20	20	1.0	4.5×10^{-2}
Hole mobility, μ_h (cm^2/Vs)	10	10	1.0	4.5×10^{-2}
Acceptor density, N_A (1/cm^3)	0	0	1.0×10^{16}	1.0×10^{18}
Donor density, N_D (1/cm^3)	1.0×10^{21}	1.0×10^{16}	1.0×10^{20}	0
Defect density, N_t (1/cm^3)	1.0×10^{15}	1.0×10^{15}	1.0×10^{12}	1.0×10^{15}
Effective density of conduction band (CB) states, N_c (1/cm^3)	2.2×10^{18}	1.0×10^{19}	1.0×10^{20}	2.2×10^{18}
Effective density of conduction band (VB) states, N_v (1/cm^3)	1.8×10^{19}	1.0×10^{19}	1.0×10^{20}	1.8×10^{19}

Table 2 Interface layer parameters

Parameter	TiO_2/BEHP-*co*-MEH-PPV interface	BEHP-*co*-MEH-PPV/PEDOT:PSS interface
Type of defect	Neutral	Neutral
Total density (1/cm^3)	1.0×10^{10}	1.0×10^{10}
Capture cross-section of electrons (cm^2)	1.0×10^{-19}	1.0×10^{-19}
Capture cross-section of holes (cm^2)	1.0×10^{-19}	1.0×10^{-19}
Reference energy (eV)	0.6	0.6

Table 3 Parameters for non-deal conditions

Parameter	BEHP-*co*-MEH-PPV [4, 19]
Defect density, N_t (1/cm^3)	1.0×10^{15}
Series resistance, R_s (Ω·cm^2)	10
Shunt resistance, R_{sh} (Ω·cm^2)	10^2
Front-surface reflection losses (%)	10
Radiative coefficient, B (cm^3/s)	3.125×10^{-10}
Auger coefficient, C (cm^6/s)	1.1221×10^{-28}
Operating temperature (K)	360

3 Results and discussion

3.1 Density functional theory results for the light absorber layer

3.1.1 Optimization of geometry

The molecular geometry of the BEHP-*co*-MEH-PPV copolymer was relaxed using DFT to minimize steric strain and establish the equilibrium conformation prior to electronic property extraction. Due to the $O(N^3)$ computational scaling of all-electron DFT with system size, a finite oligomer approximation was employed [20]. A BEHP-PPV:MEH-PPV monomer ratio of 3:2 was selected instead of the nominal 6:4 composition to maintain tractable basis set dimensions while preserving the statistical copolymer sequence and effective conjugation length. This finite-chain approach is a standard and validated strategy in computational organic photovoltaics for capturing local backbone torsional dynamics and side-chain packing without introducing periodic boundary artifacts [21]. Fig. 2 displays the fully optimized oligomer geometry. The relaxation process resolves initial steric conflicts between the bulky 2-ethylhexyloxy (BEHP) and 2-methoxy-5-(2-ethylhexyloxy) (MEH) side groups, allowing the phenylene-vinylene backbone to adopt a semi-planar conformation that maximizes π-orbital overlap. The optimized structure shows short non-covalent interatomic contacts of approximately 2.440 Å and 2.393 Å, corresponding to weak intramolecular O···H interactions. The side chains enhance structural stability and processability, while weak intramolecular O···H contacts help stabilize the optimized conformation [22].

3.1.2 Energy calculation

The DFT geometry optimization converged successfully after 10 SCF iterations with a tolerance of 0.001853 eV. The total DFT-D energy of the optimized BEHP-*co*-MEH-PPV oligomer (1000 electrons) is −151,741.36 eV or -2.43×10^{-14} J. The binding energy of −1448.89 eV confirms the thermodynamic stability of the relaxed copolymer structure. The DFT-D dispersion correction contributed −12.4432 eV to the total energy, accounting for van der Waals interactions critical for modeling the steric packing of the alkoxy side chains [10].

3.1.3 HOMO LUMO analysis

The frontier molecular orbital energies were extracted directly from the converged DFT eigenvalues. The highest occupied molecular orbital (HOMO) and lowest unoccupied molecular orbital (LUMO) correspond to eigenvalues of −3.95 eV and −2.49 eV, respectively. The energy bandgap, ΔE, is subsequently determined as 1.452 eV. The isosurface distributions in Fig. 3 demonstrate that both the HOMO and LUMO are strongly delocalized along the conjugated phenylene–vinylene backbone, with negligible electron density on the alkoxy side chains. This extensive π-orbital overlap confirms that the geometry optimization successfully preserved backbone planarity, thereby maximizing the effective conjugation length. Such delocalization is critical for facilitating intramolecular charge transport and reducing the exciton binding energy, which typically ranges from 0.3 to 0.5 eV in conjugated polymers.

It is well-established that semi-local GGA functionals (e.g., PBE) systematically underestimate band gaps of conjugated polymers on the order of 0.3–0.7 eV, due to the absence of the exchange-correlation derivative discontinuity and exact exchange [23–25]. The calculated frontier orbital energies are in reasonable agreement with experimentally determined energy levels of MEH-PPV-based conjugated polymers obtained from cyclic voltammetry

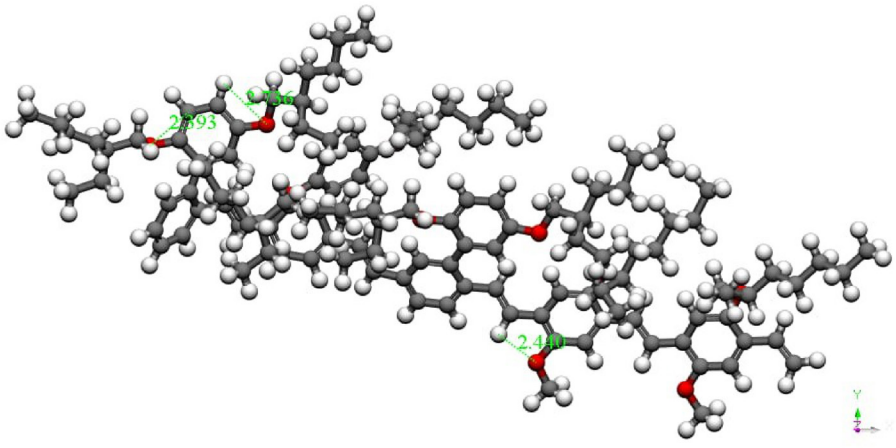

Fig. 2 Optimized geometry of BEHP-*co*-MEH-PPV optimized at PBE functional. The grey color is carbon, white color is hydrogen and red color is oxygen.

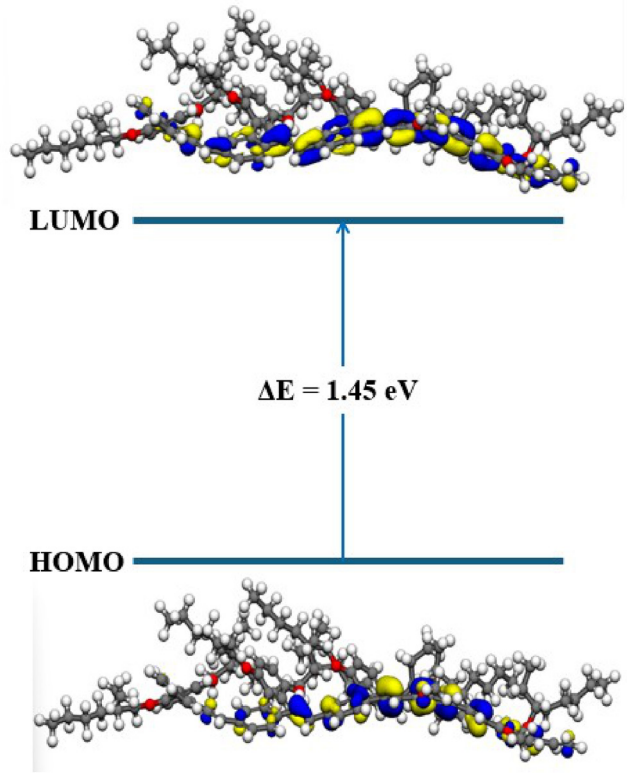

Fig. 3 HOMO and LUMO orbitals of BEHP-*co*-MEH-PPV

and ultraviolet photoelectron spectroscopy, confirming that the calculations reproduce the expected electronic structure of this class of materials [26, 27]. Experimental optical gaps for PPV-based copolymers generally fall between 2.0 and 2.4 eV [28]. However, the calculated band gap (1.45 eV) is lower than experimentally reported optical gaps. For this device modeling purposes, we used the experimentally reported bandgap of 2.12 eV [5, 29], which lies within the GGA:PBE functional underestimation (0.67 eV). Thus, the DFT calculations are used primarily to validate the optimized molecular geometry and the relative frontier orbital characteristics, whereas the SCAPS-1D simulations employ the experimentally measured optical band gap (2.12 eV) to ensure physically realistic device modeling.

3.1.4 Optical absorption

Fig. 4 presents the optical absorbance spectrum of the BEHP-*co*-MEH-PPV copolymer obtained from the DFT calculations. The spectrum exhibits multiple absorption bands across the visible region (480–730 nm), characteristic of conjugated polymer systems. Moderate absorption peaks are observed near 505 nm, 530 nm, and 658 nm, while the strongest absorption occurs at approximately 713 nm with an oscillator strength of about 1.7. The prominent absorption peak corresponds to the π–π^* transition

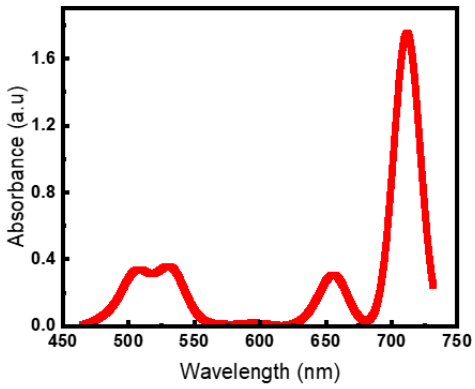

Fig. 4 Absorption spectra of BEHP-*co*-MEH-PPV

of the conjugated backbone, which is consistent with the calculated HOMO–LUMO gap [30, 31]. The additional vibronic shoulders at shorter wavelengths indicate interchain interactions and conformational ordering within the copolymer structure [32]. The broad absorption profile extending into the visible region demonstrates the material's potential for harvesting solar photons, particularly in the green–orange spectral range where solar irradiance is substantial.

3.1.5 Density of states

Fig. 5 presents the total density of states (DOS) spectrum of the BEHP-co-MEH-PPV copolymer calculated from DFT. The DOS profile reveals distinct electronic states distributed across the energy spectrum, with the Fermi level positioned at 0 eV. Sharp peaks at approximately 9.7 eV (C 1s) and 18.5 eV (O 1s) originate from atomic core electrons, which are highly localized and energetically distinct, while the multiple peaks between 1.0 eV and 0 eV in the valence band reflect various bonding and antibonding π-orbitals of the conjugated backbone [31]. Although DMol3 applies Gaussian broadening to smooth these discrete levels into continuous-looking curves, the

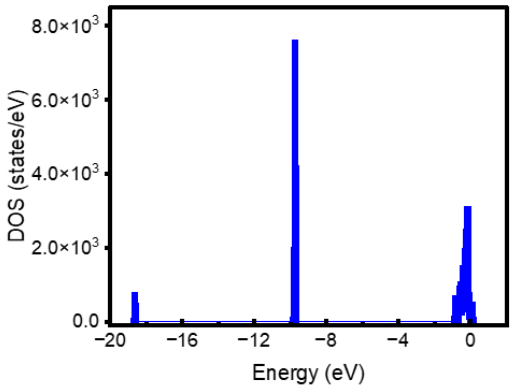

Fig. 5 Density of states of BEHP-*co*-MEH-PPV

underlying data remains discrete [33]. The calculated DOS shows a flat plateau near the Fermi level, which should not be interpreted as evidence of physical mid-gap defects or trap-assisted recombination centers. Instead, this feature arises from the finite-size oligomer approximation and Gaussian broadening applied for visualization purposes. Real materials do not show ideal discrete spikes because solution-processed polymers contain conformational disorder, which naturally broadens states into continuous bands [34, 35]. In SCAPS-1D simulations, a Gaussian defect distribution (Urbach tail) centered within the bandgap is usually introduced, with a volumetric defect density (N_t) and capture cross-section derived from literature on disordered PPV systems. This approach bridges the molecular-scale electronic structure with the macroscopic trap-assisted recombination kinetics, ensuring physically realistic device modeling [36, 37].

3.2 Solar cell capacitance simulator, 1-dimension results of the solar cell

3.2.1 Validation of the solar cell

Fig. 6 presents the baseline electrical and optoelectronic characteristics of the inverted FTO/TiO_2/BEHP-*co*-MEH-PPV/PEDOT:PSS/Au architecture under AM1.5G illumination (100 mW/cm^2, 300 K). Fig. 6(a) shows the current density–voltage (J–V) response, where the dark curve exhibits ideal rectifying behavior with negligible reverse-bias leakage, confirming high shunt resistance and effective interfacial passivation. Under illumination, the device yields an open-circuit voltage (V_{oc}) of 1.229 V, a short-circuit current density (J_{sc}) of 9.018 mA/cm^2, and a fill factor (FF) of 86.95%, corresponding to a power conversion efficiency (PCE) of 9.63%. These parameters are consistent with the illuminated single-diode model:

$$J = J_0\left[\exp\left(\frac{qV}{\eta kT}\right)-1\right] \tag{4}$$

wherein J_0 represents the saturation current density, q the elementary charge, η the ideality factor, k Boltzmann's constant, and T the absolute temperature [38].

The external quantum efficiency (QE) spectrum in Fig. 6(b) shows an optical absorption profile between 300 nm and 700 nm. The spectral roll-off beyond 700 nm confirms that photon harvesting is efficiently converted into extracted carriers without significant recombination losses [39]. The absorption features predicted by DFT are consistent with the QE spectrum, validating the optical behavior of the BEHP-*co*-MEH-PPV absorber.

Fig. 6(c) displays the equilibrium energy band diagram across the device stack. The SCAPS-1D simulation shows a standard n-i-p organic photovoltaic structure with favorable type-II staggered heterojunction alignment at both the TiO_2/polymer and polymer/PEDOT:PSS interfaces. The device exhibits significant band bending in the polymer layer near TiO_2, establishing a built-in electric field that drives charge separation. Electrons flow toward TiO_2 (collected at FTO) while holes flow toward PEDOT:PSS

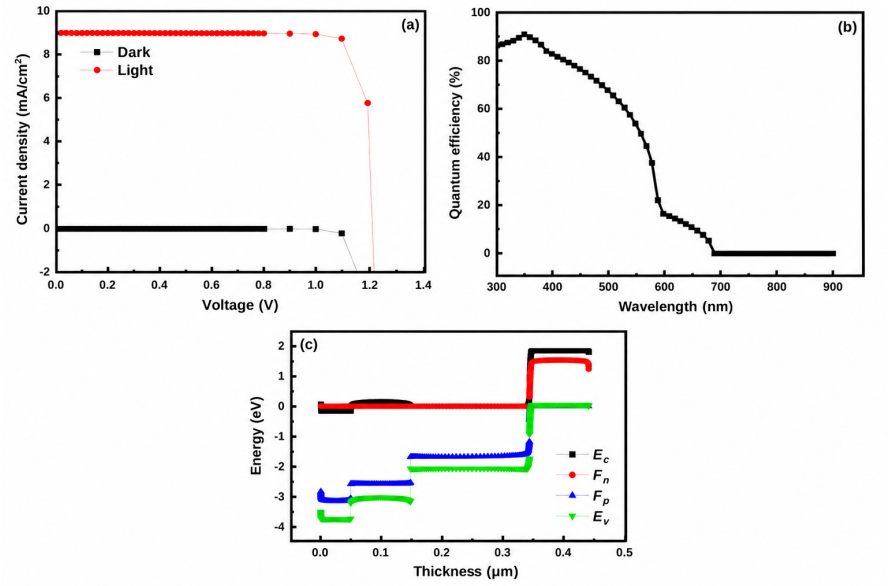

Fig. 6 Reference CSC device (a) current density–voltage curve, (b) quantum efficiency curve, (c) energy band (where E_c = conduction band edge, E_v = valence band edge, F_n = quasi-Fermi level of electron, and F_p = quasi-Fermi level of hole)

(collected at Au). The main limitation is the large 1.2 eV conduction band offset at the TiO_2/polymer interface, which sacrifices open-circuit voltage. This band alignment validates the suitability of the inverted architecture's for stable, solution-processed organic photovoltaics prior to systematic thickness-dependent analysis [40].

3.2.2 Absorber thickness effect on defect density

Fig. 7 reveals the profound influence of film thickness on the defect landscape and device performance. The defect density N_t, which quantifies the concentration of trap states within the bandgap, is a critical parameter governing the recombination kinetics and ultimately the power conversion efficiency of the solar cell. At 0.1 µm thickness, the device achieves V_{oc} = 1.220 V, J_{sc} = 7.08 mA/cm^2, FF = 86.6%, yielding PCE = 7.49%. Upon increasing the thickness to 1 µm, the Voc decreases to 1.210 V, J_{sc} drops to 4.90 mA/cm^2, while FF remains relatively stable at 86.4%, resulting in PCE = 5.12%. This 31% reduction in PCE with increasing thickness is directly attributable to enhanced recombination losses associated with the higher effective defect density in thicker films [41, 42].

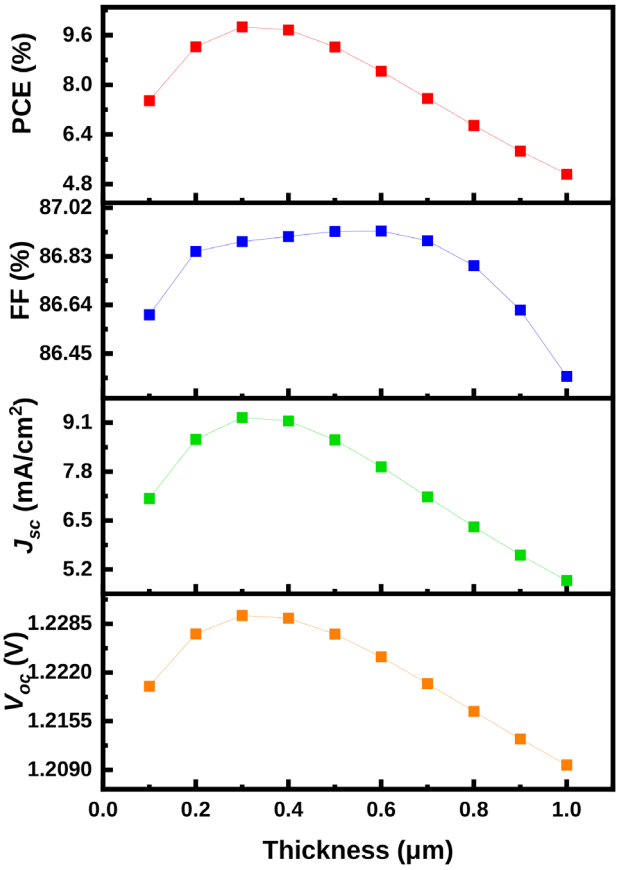

Fig. 7 Device performance of active layer thickness *vs* defect density

The physical mechanism underlying this observation can be described by the Shockley-Read-Hall (SRH) recombination formalism, wherein the recombination rate R_{SRH} is proportional to the trap density N_t:

$$R_{SRH} = \frac{pn - n_i^2}{\tau_p\left(n + n_1\right) + \tau_n\left(p + p_1\right)} \tag{5}$$

where τ_p and τ_n are the minority carrier lifetimes, and n_1 and p_1 are the SRH statistics parameters. As the active layer thickness increases, the total number of bulk defects integrated across the film increases, leading to shorter effective carrier lifetimes and increased non-geminate recombination. Furthermore, the longer carrier transit distances in thicker films aggravate space-charge accumulation, which distorts the internal electric field distribution and degrades charge collection efficiency [43].

The inverse relationship between J_{sc} and thickness observed herein is consistent with the Hecht framework for disordered organic semiconductors, wherein the charge collection probability η_{cc} follows:

$$\eta_{cc} \propto \frac{\mu\tau E_0}{L} \tag{6}$$

where μ_τ is the mobility-lifetime product, E_0 is the built-in field, and L is the active layer thickness. As L increases beyond the characteristic diffusion length, charge collection deteriorates exponentially [42].

3.2.3 Thickness effect on parasitic resistances

The introduction of a substantial series resistance imposes a severe voltage drop across the device, governed by $\Delta V = J \cdot R_s$. As shown in Fig. 8(a), while the J_{sc} and V_{oc} follow a uniform increase with thickness due to enhanced optical generation, the FF exhibits a critical degradation and gradually drops as thickness increases. This behavior is dictated by the normalized series resistance:

$$r_s = \frac{R_s J_{sc}}{V_{oc}} \tag{7}$$

At high thicknesses, the interplay between the high Rs and the specific charge extraction dynamics creates a severe mismatch, suppressing the *J–V* curve. Although J_{sc} increases with thickness, the absolute resistive loss (I^2R_s) remains a dominant bottleneck, capping the PCE well below the intrinsic potential of the BEHP-*co*-MEH-PPV copolymer.

Fig. 8(b) reveals the catastrophic impact of a low shunt resistance, which introduces a parallel leakage current path:

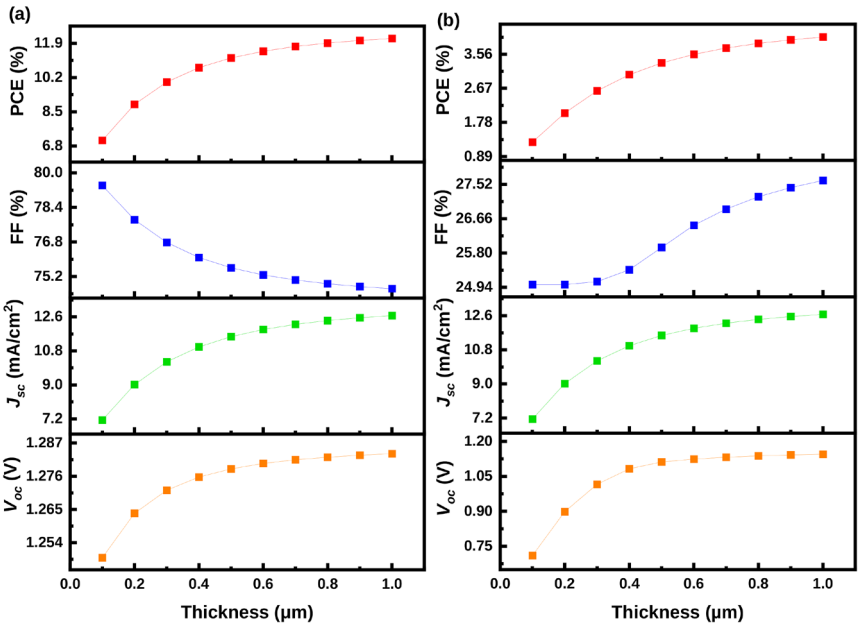

Fig. 8 Device performance of active layer thickness *vs* (a) series resistance, (b) shunt resistance

$$J_{\text{leak}} = \frac{Voc}{R_{sh}} \tag{8}$$

For R_{sh} = 100 Ω.cm^2 and V_{oc} = 1.24 V, the leakage current at open circuit is J_{leak} = 12.4 mA/cm^2. Since this leakage exceeds the photogenerated current, J_{sc} = 7.14 mA/cm^2 at 0.1 μm, the condition $r_{sh} < 1$ is met, resulting in a purely ohmic *J*–*V* characteristic with no rectifying knee. As the active layer thickness increases to 1.0 μm, J_{sc} rises to 12.67 mA/cm^2, significantly improving rsh and allowing the FF to recover. Nevertheless, the PCE remains severely suppressed, demonstrating that mitigating shunt paths is a prerequisite for any viable thick-film organic solar cell architecture [44].

Figs. 9(a) and 9(b) illustrate the small-signal capacitance–voltage (*C*–*V*) characteristics of the BEHP-*co*-MEH-PPV devices under a relatively high series resistance and a low shunt resistance, respectively. These

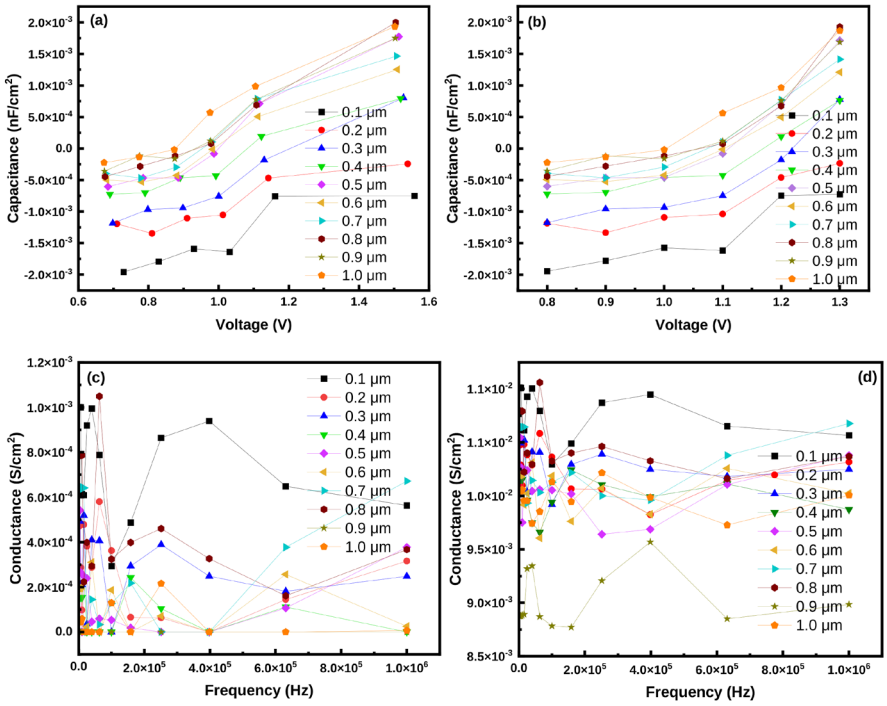

Fig. 9 Active layer thickness *vs* (a) series resistance capacitance, (b) shunt resistance capacitance, (c) series resistance conductance, (d) shunt resistance conductance

profiles provide valuable insights into the charge storage mechanisms and electrostatic behavior of the active layer. The high series resistance limits carrier transport under forward bias, whereas the low shunt resistance introduces leakage pathways that influence the measured capacitance, particularly at low bias. Nevertheless, the observed thickness dependence remains primarily governed by the electrostatic properties of the absorber.

Under reverse bias and low forward bias ($V < V_{bi}$), the device remains predominantly in the depletion regime, and the measured capacitance is primarily determined by the depletion capacitance, which approaches the geometric capacitance when the active layer is substantially depleted. the simulated results show that thinner active layers (0.1 μm) exhibit larger capacitance than thicker layers (1.0 μm). This behavior is consistent with the active layer being substantially depleted, such that the measured capacitance approaches the geometric capacitance [45].

As the applied bias approaches and exceeds the built-in potential ($V_{bi} \approx 1.3$ V), the capacitance increases rapidly for all active-layer thicknesses, indicating the transition from the depletion regime to the carrier injection regime. In this region, the measured capacitance becomes increasingly dominated by the chemical (diffusion) capacitance associated with the accumulation of injected carriers within the available density of states. The chemical capacitance is given by

$$C_{\mu} = \frac{q^2}{k_B T} \int g(E) f(E) \left[1 - f(E)\right] dE \,, \tag{9}$$

where $g(E)$ is the density of electronic states and $f(E)$ is the Fermi–Dirac distribution function. Under forward bias, injected carriers occupy the available density of states, including band-tail and trap states, leading to enhanced charge accumulation and the pronounced increase in capacitance observed in the simulations [46].

The presence of parasitic resistances modulates the effective voltage distribution. In Fig. 9(a), the high R_s introduces a significant ohmic voltage drop, $\Delta\text{drop} = J \cdot R_s$, which reduces the effective potential across the active layer, shifting the onset of the capacitive rise to higher applied voltages. Conversely, in Fig. 9(b), the low R_{sh} introduces leakage currents that compete with the displacement current. Under alternating current (AC) analysis, this leakage increases the dielectric loss tangent:

$$\tan\delta = \frac{1}{\omega R_{sh} C} \,, \tag{10}$$

(where ω is the angular frequency), which can flatten the C–V response or introduce artifacts related to the dielectric relaxation time $\tau = R_{sh}C$ [45]. Nevertheless, the distinct separation of the curves based on thickness in both scenarios confirms that while parasitic elements degrade the direct current (DC) power output, the fundamental electrostatic scaling remains robust.

In Fig. 8(c), the series conductance, G_s, exhibits a pronounced dispersion at low frequencies, particularly for thicker active layers. This behavior is characteristic of trap-limited charge transport in disordered organic semiconductors. At low frequencies, the alternating field period exceeds the characteristic trap emission time of carriers from deep trap states (τ_t), allowing trapped charges to be released and contribute to conduction. With increasing frequency, trapped carriers cannot respond to the alternating field and are effectively immobilized on the timescale of the measurement, leading to a reduced effective conductivity dominated by mobile carriers in extended or hopping transport states. The marked increase in low-frequency G_s with thickness confirms that thicker films possess a higher volumetric density of active trap states, worsening resistive losses [46, 47]. Conversely, the shunt conductance, G_{sh}, represents the leakage current pathways and dielectric losses across the junction. Here, the G_{sh} profiles exhibit a complex, non-linear frequency dependence, showing thickness-dependent fluctuations and localized peaks at low frequencies. This is indicative of slow kinetic processes, such as interface-mediated recombination or the response of deep-level trap states [45]. However, as the frequency increases, G_{sh} demonstrates a marked upward trend across most active layer thicknesses. This high-frequency dispersion is characteristic of AC hopping conductivity and dielectric relaxation phenomena in disordered organic semiconductors, governed by Jonscher's universal power law:

$$G_{sh}(\omega) = G_{dc} + A\omega^{s} \,, \tag{11}$$

where G_{dc} is the DC shunt conductance, and $A\omega^s$ accounts for the frequency-dependent losses due to charge carrier hopping between localized states [48].

3.2.4 Thickness effect on reflection losses

Figs. 10(a) and 10(b) present the illuminated J–V characteristics and external quantum efficiency spectra, respectively. As the active layer thickness increases, the J_{sc} exhibits a consistent enhancement, rising from 6.43 mA/cm^2 at 0.1 μm to 11.40 mA/cm^2 at 1.0 μm. This optical behavior

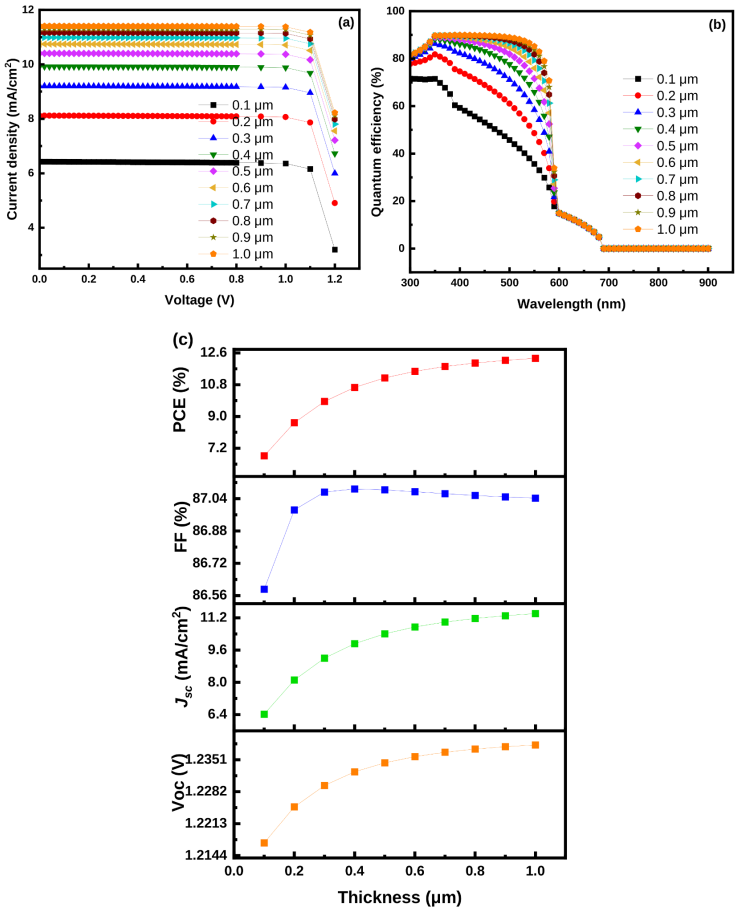

Fig. 10 Active layer thickness *vs* 10% reflectance (a) current density–voltage curve, (b) quantum efficiency curve, and (c) device performance

is governed by the Beer-Lambert law, where the spatially resolved photogeneration rate $G(x)$ is defined as:

$$G(x) = \Phi_0 (1-R)\alpha \exp(-\alpha x) \tag{12}$$

where Φ_0 is the incident photon flux, R is the reflection coefficient, and α is the absorption coefficient. In ultra-thin configurations, a significant fraction of incident photons is transmitted without absorption. Increasing the film thickness expands the optical path length, thereby compensating for the 10% reflection loss by harvesting a greater volume of sub-bandgap and near-bandgap photons [49]. Critically, the electrical extraction remains highly efficient despite the increased physical thickness. As shown in Fig. 10(c), the FF remains remarkably stable at ~87.0% across the entire thickness range, while the V_{oc} shows a marginal increase from 1.23 V to 1.24 V. The sustained high FF indicates that the charge carrier diffusion length ($LD = \sqrt{D\tau}$) in the optimized BEHP-*co*-MEH-PPV copolymer is sufficiently large relative to the 1.0 μm active layer, allowing photogenerated carriers to be extracted before significant recombination occurs. This reflects a favorable balance between transport and recombination processes, which typically deteriorate in thick disordered conjugated polymer systems due to reduced mobility and increased recombination probability [50]. Consequently, the PCE scales favorably with thickness, peaking at 12.29% for the 1.0 μm device. These results demonstrate that, unlike conventional PPV derivatives, which are strictly limited to active layers below 0.1 μm due to low mobility, this specific copolymer formulation permits the use of optically thick layers. This capability is essential for offsetting realistic reflection losses in scalable, large-area manufacturing without compromising the electrical collection efficiency required for tropical deployment [51].

3.2.5 Thickness effect on radiative and Auger recombination

Figs. 11(a) and 11(b) illustrate the thickness-dependent performance of the photovoltaic parameters under recombination constraints. Under a high radiative recombination coefficient (R_{rad}), B, the device performance is governed by bimolecular losses, defined by the rate equation:

$$R_{rad} = B\left(np - n_i^2\right) \tag{13}$$

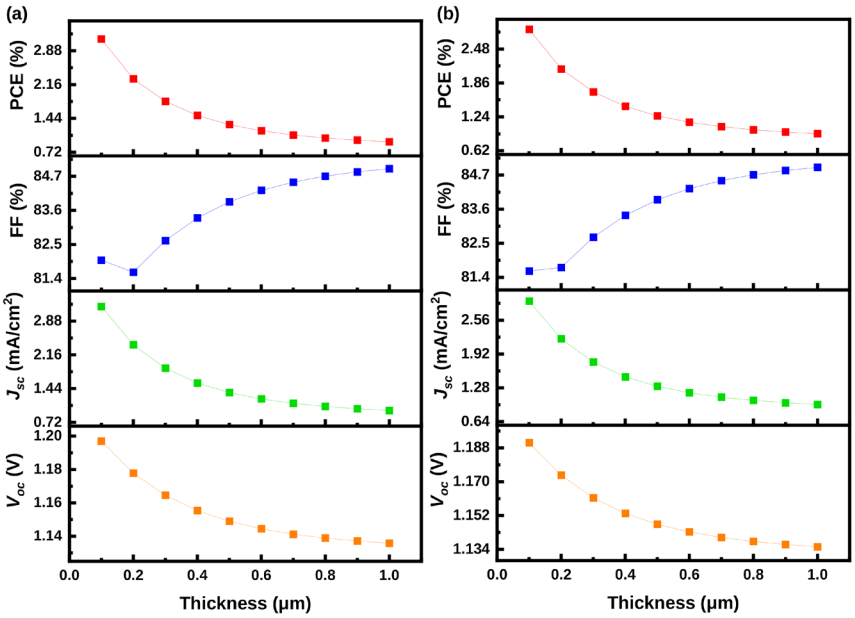

Fig. 11 Device performance of active layer thickness *vs* (a) radiative recombination, (b) Auger recombination

As the active layer thickness increases from 0.1 μm to 1.0 μm, the J_{sc} and V_{oc} exhibit a uniform decline. This degradation is attributed to the reduced charge collection probability in thicker films. When the film thickness exceeds the effective diffusion length, carrier extraction becomes diffusion-limited and recombination dominates over charge collection [52]. Consequently, the steady-state carrier density is suppressed, leading to a collapse in V_{oc}. Notably, the FF displays an anomalous increasing trend, rising from 82% to 85%. This behavior suggests a transition in the dominant loss mechanism. In ultra-thin films, the high carrier extraction rate, combined with intense radiative recombination, may create a system where the recombination current rivals the photocurrent, severely flattening the *J–V* curve [40]. The PCE consequently degrades, confirming that high radiative losses strictly bound the viable thickness for this copolymer.

Fig. 11(b) presents the device characteristics under a dominant Auger recombination structure, where the electron–hole recombination energy is transferred to an additional carrier:

$$R_{\text{Auger}} = C_n n^2 p + C_p n p^2 \tag{14}$$

The trends mirror those of the radiative limit but are more severe due to the non-linear dependence of Auger losses on carrier density. In thicker films, the internal electric field is distributed over a larger distance, reducing the drift velocity and causing carrier accumulation due to the low bulk mobility of the copolymer. According to the recombination kinetics framework established by Kirchartz et al. [53], this accumulation of steady-state carrier density (n) governs the bulk recombination rate, $R \propto n^{\alpha}$, where α is the recombination order. As the carrier density increases, bulk recombination becomes increasingly significant due to this nonlinear dependence. In the specific case of the simulated extreme Auger limit, this carrier pile-up triggers a massive surge in non-radiative losses, severely compressing the quasi-Fermi level splitting and leading to a sharp decline in both J_{sc} and V_{oc}. The PCE drops precipitously with thickness, indicating that Auger processes are a critical bottleneck for thick-film organic photovoltaics. The FF again shows an increasing trend, likely because, just as in the radiative recombination, the drastic reduction in J_{sc} minimizes the impact of series resistance, improving the squareness of the *J–V* curve even as the total power output vanishes.

Figs. 12(a) and 12(b) illustrate the Shockley-Read-Hall recombination current density (J_{SRH}) when the device is constrained by extreme radiative and Auger coefficients, respectively. Counter-intuitively, J_{SRH} exhibits a decreasing trend with increasing active layer thickness, dropping from 0.31 mA/cm^2 at 0.1 μm to 0.11 mA/cm^2 at 1.0 μm. This occurs because the artificially high bimolecular and triplet recombination rates severely deplete the steady-state free carrier concentrations (n, p) within the bulk. Consequently, the carrier population available to be captured by mid-gap trap states is drastically reduced, suppressing the integrated SRH loss:

$$J_{\text{SRH}} = q\int_0^d \frac{np - n_i^2}{\tau_p\left(n + n_1\right) + \tau_n\left(p + p_1\right)} dx\,, \tag{15}$$

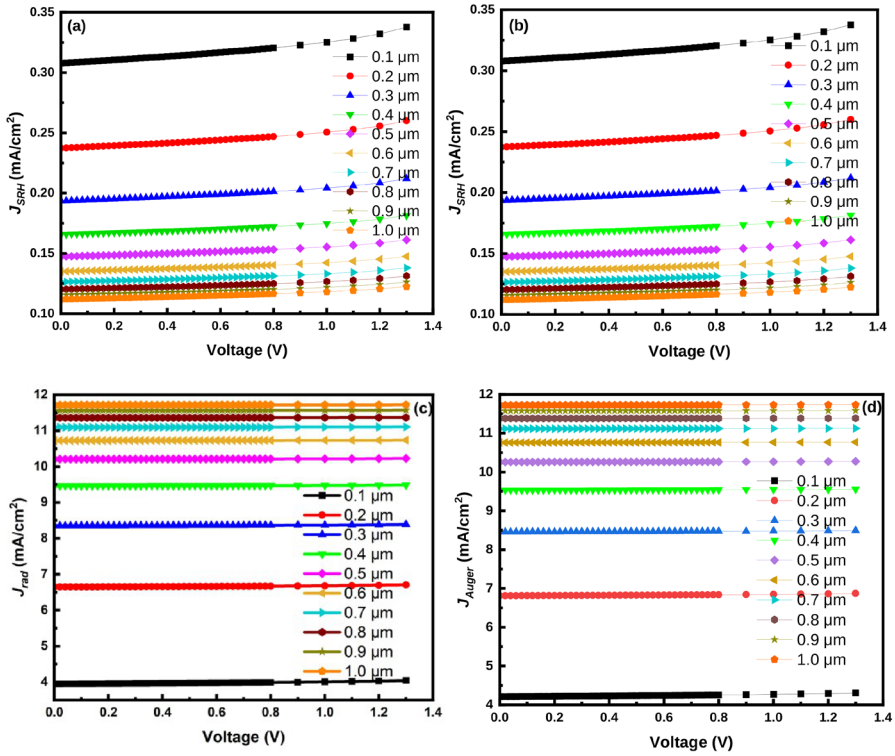

Fig. 12 Active layer thickness *vs* (a) radiative SRH recombination current density, (b) Auger SRH recombination current density, (c) radiative recombination current density, (d) Auger recombination current density

where the rapid depletion of n and p by the dominant intrinsic channels minimizes the SRH integrand [40]. Conversely, Figs. 12(c) and 12(d) reveal a pronounced, consistent increase in the intrinsic recombination currents. The radiative recombination current (J_{rad}) scales from 3.95 mA/cm^2 to 11.72 mA/cm^2 as the thickness increases to 1.0 µm. This is governed by the volumetric integration of the bimolecular rate:

$$J_{rad} = q\int_0^d B\left(np - n_i^2\right)dx \tag{16}$$

The thicker active layer harvests more photons, increasing the total photogenerated carrier population and the integration volume, thereby elevating the total radiative loss [54]. Similarly, the Auger recombination current (J_{Auger}) rises from 4.22 mA/cm^2 to 11.73 mA/cm^2. Auger recombination is a three-carrier process highly sensitive to carrier density:

$$J_{\text{Auger}} = q\int_0^d \left(C_n n^2 p + C_p n p^2\right)dx \tag{17}$$

These results confirm that under intrinsic limits, the performance degradation in thick BEHP-*co*-MEH-PPV films is driven primarily by bimolecular and Auger recombination rather than trap-assisted SRH losses.

3.2.6 Thickness effect on temperature

Fig. 13 illustrates the performance of the photovoltaic parameters as a function of active layer thickness under a realistic operating temperature peak of 360 K (87 °C) characteristic of typical tropical African climates. The J_{sc} exhibits a constant increase, rising from 7.16 mA/cm^2 at 0.1 µm to 12.69 mA/cm^2 at 1.0 µm. Here, thicker films harvest a greater volume of incident photons, directly boosting the photocurrent despite the thermal energy. The V_{oc} shows a marginal increase from 1.20 V to 1.22 V. Typically, elevated temperatures suppress V_{oc} due to the exponential rise in J_0 and the narrowing of the bandgap (Varshni effect) [55]. However, the relation:

$$V_{oc} = \frac{nkT}{q}\ln\left(\frac{J_{sc}}{J_0}+1\right) \tag{18}$$

indicates that the substantial gain in J_{sc} at larger thicknesses partially compensates for the thermal increase in J_0. The observed V_{oc} behavior is consistent with the interplay between the temperature dependence of J_0, enhanced photogeneration, and recombination dynamics [56]. The FF rises sharply in the ultra-thin structure before saturating at 84%. The low FF in thin films is often attributed to dominant interface recombination or shunt leakage paths. As the active-layer thickness

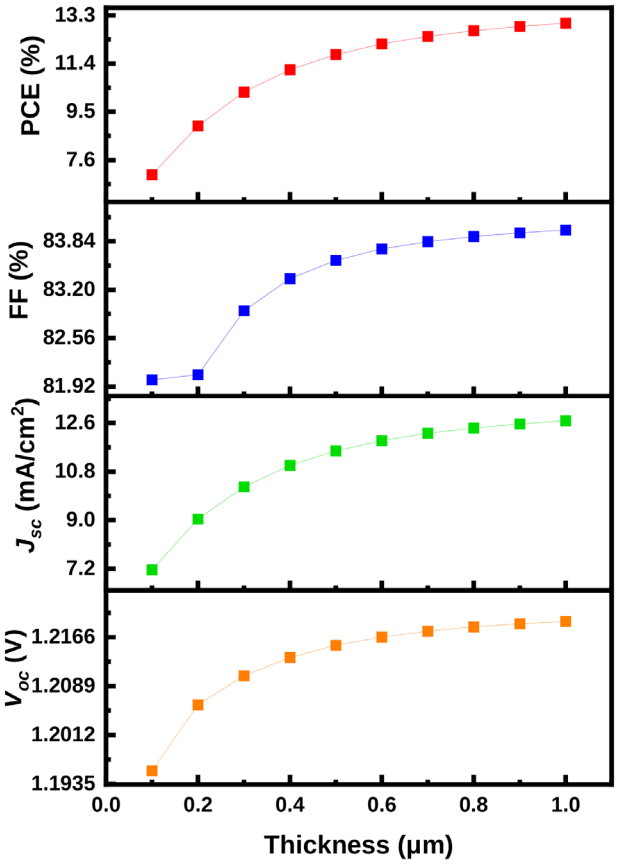

Fig. 13 Device performance of active layer thickness *vs* temperature

increases, bulk transport begins to dominate device operation and the relative influence of interfacial losses is reduced, allowing the fill factor to recover and remain nearly constant over an intermediate thickness range [43]. This suggests that the charge carrier diffusion length in the BEHP-*co*-MEH-PPV copolymer is sufficient to support efficient extraction even at 360 K. Consequently, the PCE mirrors the J_{sc} trend, increasing from 7.0% to 13.0%. Thus, while high operating temperatures impose a thermodynamic penalty, optimizing the active layer thickness to maximize photon absorption remains a critical strategy for sustaining high efficiency in hot environments.

3.2.7 Comparison under ideal conditions

Under ideal conditions (Fig. 14(a)), where bulk trap densities are negligible and recombination is strictly limited to intrinsic radiative processes, the device exhibits optimal performance characteristics. As the thickness increases to 1.0 μm, J_{sc} rises consistently to 12.67 mA/cm^2, driven by enhanced optical absorption. Crucially, the V_{oc} remains stable at 1.24 V, and the FF maintains a high value of 87%. This stability confirms that in the absence of mid-gap traps, the charge carrier diffusion length far exceeds the active layer thickness, ensuring near-unity charge collection efficiency even in optically thick films [57]. When compared with this optimized device performance, experimental devices based on pristine BEHP-*co*-MEH-PPV typically exhibit lower photovoltaic parameters, with reported PCE values generally below 2%. Anything above this range usually falls within the category of doped or BEHP-*co*-MEH-PPV hybrid active layers, as presented in Table 4.

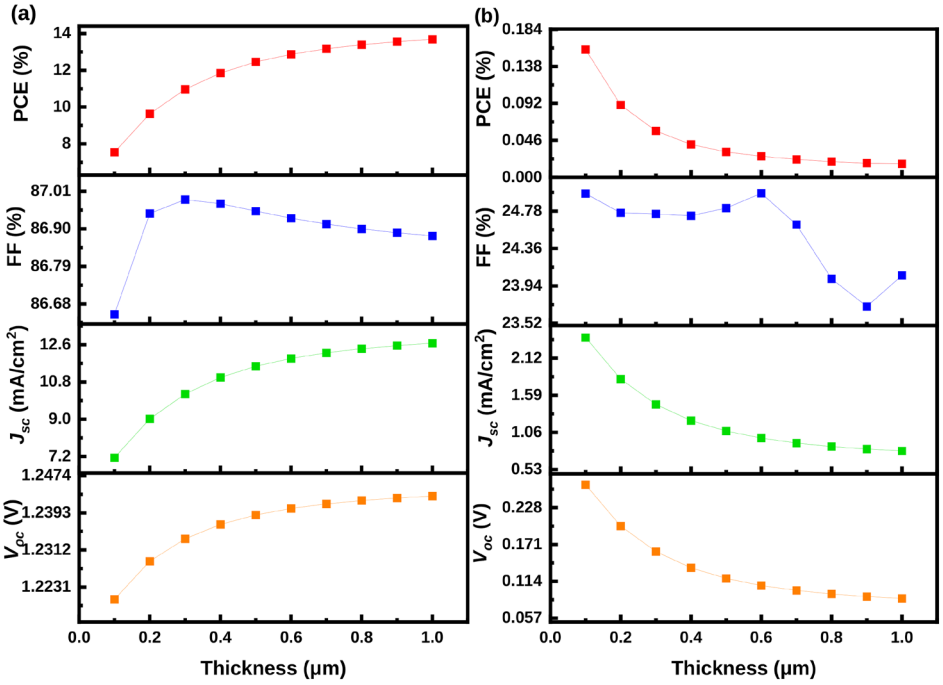

Fig. 14 Device performance of active layer thickness under (a) ideal conditions, (b) nonideal conditions

Table 4 Comparison of ideal BEHP-*co*-MEH-PPV device with previous works

References	V_{oc} (V)	J_{sc} (mA/cm^2)	FF (%)	PCE (%)
[3]	0.53	1.02	66.5	0.36
[5]	0.27	2.66	38	3
[2]	1.15	5.54	75.80	4.86
[4]	1.31	8.29	69.47	7.52
This work	1.24	12.67	87	13.69

The higher simulated performance is expected because the numerical model assumes idealized material quality, optimized layer thicknesses, defect density, carrier mobility, and interfacial properties while neglecting several loss mechanisms present in practical devices, including morphological disorder, interface trap states, series resistance, contact imperfections, exciton quenching, and fabrication-induced defects. Consequently, the simulated results should be regarded as the theoretical performance limit achievable under optimized conditions rather than a direct reproduction of current experimental devices.

Conversely, Fig. 14(b) exposes the severe performance degradation under non-ideal conditions, incorporating realistic bulk defect densities typical of disordered conjugated polymers. As the thickness shifts towards 1.0 µm, the FF collapses catastrophically from 25% to 23.71%, while J_{sc} plummets to a mere 0.82 mA/cm^2. This degradation is fundamentally governed by the dominance of SRH trap-assisted recombination. In thick films, the charge carrier transit time scales quadratically with thickness. When the carrier movement exceeds the trap-limited lifetime (τ_{SRH}), photogenerated carriers experience increased trap-assisted recombination before reaching the selective contacts [53]. This massive bulk recombination not only depletes the steady-state carrier population (thereby suppressing V_{oc}) but also introduces severe resistive losses manifesting as the observed collapse in FF [40]. The stark contrast between Figs. 14(a) and 14(b) highlights a critical design rule for scalable organic photovoltaics whereby simply increasing the active layer thickness to maximize photon harvesting is futile unless the charge carrier mobility is enhanced or the defect density is drastically suppressed. For the BEHP-*co*-MEH-PPV device, optimizing the film thickness to balance the optical absorption depth with the effective charge collection length becomes a necessity to prevent non-ideal transport losses from negating the optical gains.

The stepwise cumulative analysis of non-ideal conditions, as shown in Table 5, starkly illustrates the compounding degradation of the BEHP-*co*-MEH-PPV device, driving the PCE from an ideal 13.69% down to a negligible 0.02%. The introduction of bulk defect density initiates a severe collapse in J_{sc} from 12.67 to 4.905 mA/cm^2 due to dominant SRH trap-assisted recombination, while the subsequent addition of series resistance primarily penalizes the FF through increased ohmic transit losses. The most catastrophic drop occurs upon introducing a low shunt resistance, which introduces massive parallel leakage currents that collapse the V_{oc} from 1.226 V to 0.489 V and decimate the FF to 24.98%, effectively destroying the junction's rectifying capability. The compounding of front-surface reflection losses further starves the device of incident photons, reducing J_{sc} to 4.012 mA/cm^2. Finally, the sequential activation of extreme radiative and Auger recombination mechanisms, coupled with thermal stress at 360 K,

Table 5 Stepwise cumulative analysis of non-ideal conditions of BEHP-*co*-MEH-PPV device at 1.0 µm

Steps	V_{oc} (V)	J_{sc} (mA/cm^2)	FF (%)	PCE (%)
Ideal device	1.24	12.67	87.0	13.69
Applying defect density	1.210	4.905	86.36	5.12
Applying defect density + series resistance	1.226	4.903	81.64	4.91
Applying defect density + series resistance + shunt resistance	0.489	4.458	24.98	0.54
Applying defect density + series resistance + shunt resistance + reflection losses	0.440	4.012	25.0	0.44
Applying defect density + series resistance + shunt resistance + reflection losses + radiative recombination	0.088	797.756	24.02	0.02
Applying defect density + series resistance + shunt resistance + reflection losses + radiative recombination + Auger recombination	0.087	789.071	24.14	0.02
Applying defect density + series resistance + shunt resistance + reflection losses + radiative recombination + Auger recombination + temperature	0.087	796.279	24.06	0.02

further annihilates the quasi-Fermi level splitting, driving V_{oc} to a mere 0.087 V and causing extreme deviations in current extraction. This demonstrates that while optical absorption is maximized at 1.0 μm, the practical viability of thick-film BEHP-*co*-MEH-PPV solar cells is strictly bottlenecked by the synergistic penalties of bulk defects, parasitic resistances, and intrinsic recombination kinetics.

The optical generation rate $G(x)$ (Fig. 15(a)) follows the Beer-Lambert law, exhibiting a sharp exponential decay from the illuminated interface ($x = 0$) as in Eq. (12).

The high initial peak confirms strong absorption by the BEHP-*co*-MEH-PPV copolymer. As thickness increases from 0.1 to 1.0 μm, the integration of this profile yields a higher total photocurrent, provided carriers are extracted. Conversely, the recombination rate $R(x)$ (Fig. 15(b)) in non-ideal conditions closely tracks the generation profile but with significantly higher magnitude due to SRH losses. The sharp peak indicates that recombination is most severe in regions of high photogeneration and carrier accumulation. In the ideal case (radiative limit), this rate is negligible ($R_{rad} << G$), allowing efficient extraction. In contrast, the non-ideal structure exhibits R_{SRH} values approaching the local generation rate G, indicating that most generated carriers recombine before reaching the electrodes, which is consistent with the collapsed FF observed in Fig. 14(b).

The spatial distribution of charge carriers reveals the extraction dynamics. Fig. 11(c) shows a high electron concentration near the electron transport layer, which decays towards the anode. This gradient is driven by the built-in potential and diffusion. In non-ideal thick films, the electron density in the bulk may increase due to trapping (space-charge effect), creating a bottleneck for transport. Fig. 11(d) exhibits the complementary profile, with holes accumulating at the hole transport layer. The separation of these profiles confirms effective charge splitting. However, under non-ideal conditions, the significant overlap of n and p in the bulk (due to low mobility and high defect density) enhances SRH recombination, directly suppressing the V_{oc}. The results thus suggest that for thicknesses above 0.5 μm, the carrier densities in the bulk become sufficient to trigger severe recombination losses, strictly limiting the viable active layer thickness for this copolymer system.

4 Conclusion

This work establishes the intrinsic optoelectronic potential and the extrinsic thickness-dependent limitations of inverted BEHP-*co*-MEH-PPV solar cells. DFT confirms a favorable fundamental bandgap with highly delocalized frontier orbitals, enabling robust visible photon harvesting. However, SCAPS-1D device simulations reveal a critical

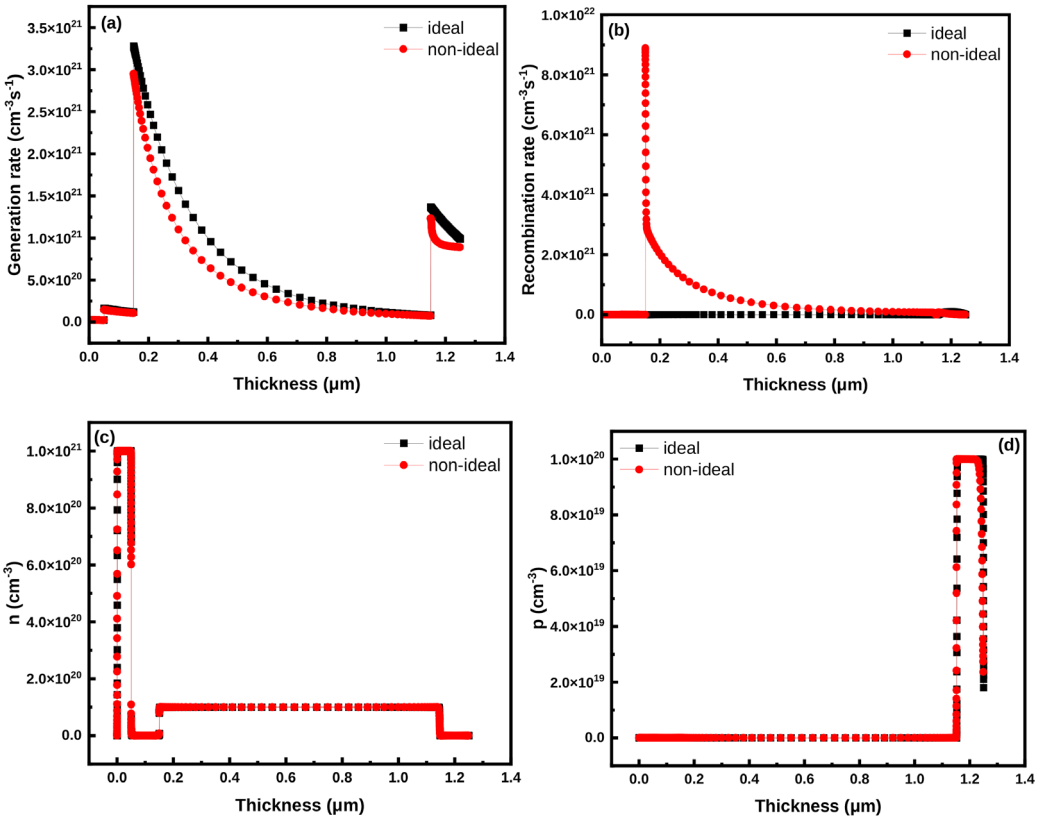

Fig. 15 Active layer thickness *vs* ideal/non-ideal (a) generation rate, (b) recombination rate, (c) electron density, (d) hole density

physical trade-off, showing that while increasing the active layer thickness enhances the J_{sc}, it simultaneously induces severe non-ideal diode behavior. The catastrophic degradation of the FF and V_{oc} in optically thick films is fundamentally governed by the dominance of Shockley-Read-Hall trap-assisted recombination and the quadratic scaling of series resistance. Furthermore, AC impedance analysis and parasitic resistance modeling confirm that trap-limited hopping and dielectric relaxation severely impede charge extraction. Although intrinsic radiative and Auger recombination impose thermodynamic boundaries, and elevated operating temperatures suppress V_{oc}, the primary bottleneck remains extrinsic defect-mediated recombination. Ultimately, while the copolymer exhibits excellent environmental stability, realizing high-efficiency, scalable thick-film devices for energy applications necessitates rigorous bulk defect passivation and charge mobility enhancement to overcome these resistive and kinetic limitations. These include using solvent additives, self-assembled monolayers, and thermal annealing to improve the material's structure, interface, and charge flow for better device performance.

Acknowledgement

Funding for this research was supported by the Central Postdoctoral Fellowship Funding at Central University of Technology, Free State, South Africa.

References

[1] Sanchez, J. C., Escobosa, A., Estrada, M. "Characterization of Thin Films of Conjugated Polymer (BEHP-PPV)-Co-(MEH-PPV) for OLEDs Aplication", In: 2006 3rd International Conference on Electrical and Electronics Engineering, Veracruz, Mexico, 2006, pp. 1–4. https://doi.org/10.1109/ICEEE.2006.251855

[2] Mahran, A. M., Abdellatif, S. O. "Optoelectronic Modelling and Analysis of Transparency against Efficiency in Perovskites/Dye-Based Solar Cells", In: 2021 International Conference on Microelectronics (ICM), New Cairo City, Egypt, 2021, pp. 178–181. https://doi.org/10.1109/ICM52667.2021.9664924

[3] Chhatre, S., Agarkar, S., Dhas, V., Nagane, S., Thakare, V., Ogale, S., Wadgaonkar, P. "Carboxyl-Modified Conjugated Polymer Sensitizer for Dye Sensitized Solar Cells: Significant Efficiency Enhancement", Journal of Materials Chemistry, 22(43), 23267, 2012. https://doi.org/10.1039/c2jm35643k

[4] Raj, A., Manocha, V., Gupta, K., Pandey, G., Sania; Raj, M., Kumar, P., Goel, N. "Machine Learning-Integrated SCAPS-1D Simulation for Optimizing N719/BEHP-Co-MEH-PPV Bilayer Dye-Sensitized Solar Cells", Physica Scripta, 100(11), 115928, 2025. https://doi.org/10.1088/1402-4896/ae1b48

[5] Mustapha, N., Ibnaouf, K. H., Fekkai, Z., Hennache, A., Prasad, S., Alyamani, A. "Improved Efficiency of Solar Cells Based on BEHP-Co-MEH-PPV Doped with ZnO Nanoparticles", Optik, 124(22), pp. 5524–5527, 2013. https://doi.org/10.1016/j.ijleo.2013.03.161

[6] Huo, M.-M., Hu, R., Zhang, Q.-S., Chen, S., Gao, X., Zhang, Y., Yan, W., Wang, Y. "Morphology and Carrier Non-Geminate Recombination Dynamics Regulated by Solvent Additive in Polymer/Fullerene Solar Cells", RSC Advances, 10(39), pp. 23128–23135, 2020. https://doi.org/10.1039/D0RA03389H

[7] Uddin, S. I., Tahir, M., Aziz, F., Sarker, M. R., Muhammad, F., Nawaz Khan, D., Hamid Md Ali, S. "Thickness Optimization and Photovoltaic Properties of Bulk Heterojunction Solar Cells Based on PFB–PCBM Layer", Energies, 13(22), 5915, 2020. https://doi.org/10.3390/en13225915

[8] BIOVIA Dassault Systèmes "BIOVIA, Materials Studio (Version 8.0)", [computer program] Dassault Systèmes, San Diego, CA, USA, 2018. Available at: https://www.3ds.com/products/biovia/materials-studio/ [Accessed: 13 February 2026]

[9] Perdew, J. P., Burke, K., Ernzerhof, M. "Generalized Gradient Approximation Made Simple", Physical Review Letters, 77(18), pp. 3865–3868, 1996. https://doi.org/10.1103/PhysRevLett.77.3865

[10] Grimme, S., Antony, J., Ehrlich, S., Krieg, H. A "Consistent and Accurate Ab Initio Parametrization of Density Functional Dispersion Correction (DFT-D) for the 94 Elements H-Pu", The Journal of Chemical Physics, 132(15), 154104, 2010. https://doi.org/10.1063/1.3382344

[11] Delley, B. "From Molecules to Solids with the DMol3 Approach", The Journal of Chemical Physics, 113(18), pp. 7756–7764, 2000. https://doi.org/10.1063/1.1316015

[12] Saidani, O., Yousfi, A., Bhattarai, S., Islame, Md. R., Sahoo, G. S. "Simulation Insights into High-Efficiency Rb2AlAgI6 Hybrid Perovskite Solar Cells: Performance Metrics and Optimization Strategies", Journal of Optics, 2025. https://doi.org/10.1007/s12596-025-02687-7

[13] El-Naggar, A. A., Eid, A. M., Rafat, Y., Khamis, M. A., Bakry, M., Elkun, S., Ismail, W., Sharshir, S. W., El-Shaer, A., Abdelfatah, M. "SCAPS Simulation and Design of Highly Efficient $CuBi_2O_4$-Based Thin-Film Solar Cells (TFSCs) with Hole and Electron Transport Layers", Scientific Reports, 15(1), 28300, 2025. https://doi.org/10.1038/s41598-025-12091-7

[14] Zouache, R., Saidani, O., Yousfi, A., Alsubaie, A. S., Soulef, B. A., Feriel, L., Islam, R. "Numerical Investigation of Enhanced Efficiency in CIGS Solar Cells with 3C-SiC and PEDOT:PSS Integration", Periodica Polytechnica Chemical Engineering, 69(1), pp. 26–34, 2025. https://doi.org/10.3311/PPch.38770

[15] Kou, X., Cheng, Y. "Performance Simulation and Optimization of Solid-State Dye-Sensitized Solar Cells Based on Novel Organic Dyes", Acta Optica Sinica, 45(11), 1125001, 2025. https://doi.org/10.3788/AOS250661

[16] Ozurumba, A. C., Ogueke, N. V., Madu, C. A. "Thermal and Electrical Analyses of Organometallic Halide Solar Cells", Journal of Solar Energy Engineering,, 146(3), 031003, 2024. https://doi.org/10.1115/1.4063808

[17] Danladi, E., Obagboye, L. F., Aisida, S., Ezema, F. I., Okorie, O., Bwamba, J. A., Emmanuel, P. A., Hussaini, A. A., Jubu, P. R.; Ozurumba, A. C. "20.730% Highly Efficient Lead-Free CsSnI3-Based Perovskite Solar Cells with Various Charge Transport Materials: A SCAPS-1D Study, Multiscale and Multidisciplinary Modeling", Experiments and Design, 8(1), 114, 2024. https://doi.org/10.1007/s41939-024-00701-2

[18] Moiz, S. A., Albadwani, S. A., Alshaikh, M. S. "Towards Highly Efficient Cesium Titanium Halide Based Lead-Free Double Perovskites Solar Cell by Optimizing the Interface Layers", Nanomaterials, 12(19), 3435, 2022. https://doi.org/10.3390/nano12193435

[19] Panachikkool, M., E T, A., Pandiyarajan, T. "Numerical Modelling of $CuBi_2O_4$ Thin Film Solar Cells with SCAPS-1D: Bridging the Gap Ideal and Non-Ideal Conditions", Materials Letters, 367, 136590, 2024. https://doi.org/10.1016/j.matlet.2024.136590

[20] Cramer, C. J. "Essentials of Computational Chemistry: Theories and Models", Wiley, 2013. ISBN 978-1-118-71227-6

[21] Brédas, J.-L., Beljonne, D., Coropceanu, V., Cornil, J. "Charge-Transfer and Energy-Transfer Processes in π-Conjugated Oligomers and Polymers: A Molecular Picture", Chemical Reviews, 2004, 104(11), pp. 4971–5004, 2004. https://doi.org/10.1021/cr040084k

[22] Beaujuge, P. M., Fréchet, J. M. J. "Molecular Design and Ordering Effects in π-Functional Materials for Transistor and Solar Cell Applications", Journal of the American Chemical Society, 133(50), pp. 20009–20029, 2011. https://doi.org/10.1021/ja2073643

[23] Gutzler, R. "Band-Structure Engineering in Conjugated 2D Polymers", Physical Chemistry Chemical Physics, 18(42), pp. 29092–29100, 2016. https://doi.org/10.1039/C6CP06101J

[24] Zhao, F., Chan, Y., Li, Z., Louie, S. G. "Excitonic Effects and Quasiparticle Band Renormalization of Poly(*p*-Phenylene Vinylene) Polymer Crystals", Physical Review B, 112(12), 125153, 2025. https://doi.org/10.1103/fvzm-j97j

[25] Perdew, J. P., Levy, M. "Physical Content of the Exact Kohn-Sham Orbital Energies: Band Gaps and Derivative Discontinuities", Physical Review Letters, 51(20), pp. 1884–1887, 1983. https://doi.org/10.1103/PhysRevLett.51.1884

[26] Sworakowski, J. "How Accurate Are Energies of HOMO and LUMO Levels in Small-Molecule Organic Semiconductors Determined from Cyclic Voltammetry or Optical Spectroscopy?", Synthetic Metals, 235, pp. 125–130, 2018. https://doi.org/10.1016/j.synthmet.2017.11.013

[27] Fischer, I., Pratt, S. T. "Photoelectron Spectroscopy in Molecular Physical Chemistry", Physical Chemistry Chemical Physics, 24(4), pp. 1944–1959, 2022. https://doi.org/10.1039/D1CP04984D

[28] Giro, R., Caldas, M. J., Galvão, D. S. "Band Gap Engineering for Poly(*p*-phenylene) and Poly(*p*-phenylene Vinylene) Copolymers Using the Tight-binding Approach", International Journal of Quantum Chemistry, 103(5), pp. 588–596, 2005. https://doi.org/10.1002/qua.20551

[29] Chasteen, S. V., Sholin, V., Carter, S. A., Rumbles, G. "Towards Optimization of Device Performance in Conjugated Polymer Photovoltaics: Charge Generation, Transfer and Transport in Poly(*p*-Phenylene-Vinylene) Polymer Heterojunctions", Solar Energy Materials and Solar Cells, 92(6), pp. 651–659, 2008. https://doi.org/10.1016/j.solmat.2008.01.014

[30] Friend, R. H., Gymer, R. W., Holmes, A. B., Burroughes, J. H., Marks, R. N., …, Salaneck, W. R. "Electroluminescence in Conjugated Polymers", Nature, 397(6715), pp. 121–128, 1999. https://doi.org/10.1038/16393

[31] Malik, A. H., Habib, F., Qazi, M. J., Ganayee, M. A., Ahmad, Z., Yatoo, M. A. A "Short Review Article on Conjugated Polymers", Journal of Polymer Research, 30(3), 115, 2023. https://doi.org/10.1007/s10965-023-03451-w

[32] Zaumseil, J. "Semiconducting Single-Walled Carbon Nanotubes or Very Rigid Conjugated Polymers: A Comparison", Advanced Electronic Materials, 5(2), 1800514, 2019. https://doi.org/10.1002/aelm.201800514

[33] Jensen, F. "Introduction to Computational Chemistry", Wiley, 2017. ISBN 978-1118825990

[34] Noriega, R., Rivnay, J., Vandewal, K., Koch, F. P. V., Stingelin, N., Smith, P., Toney, M. F., Salleo, A. A "General Relationship between Disorder, Aggregation and Charge Transport in Conjugated Polymers", Nature Materials, 12(11), pp. 1038–1044, 2013. https://doi.org/10.1038/nmat3722

[35] Botiz, I., Stingelin, N. "Influence of Molecular Conformations and Microstructure on the Optoelectronic Properties of Conjugated Polymers", Materials, 7(3), pp. 2273–2300, 2014. https://doi.org/10.3390/ma7032273

[36] Jeon, J., Yamanaka, K., Saito, M., Osaka, I., Ohkita, H., Kim, H. D. "Competition Between Charge Collection and Recombination Governing the Fill Factor in Phase-Separated All-Polymer Solar Cells", Advanced Functional Materials, 36(36), e30703, 2026. https://doi.org/10.1002/adfm.202530703

[37] Vandewal, K., Benduhn, J., Nikolis, V. C. "How to Determine Optical Gaps and Voltage Losses in Organic Photovoltaic Materials", Sustainable Energy & Fuels, 2(3), pp. 538–544, 2018. https://doi.org/10.1039/C7SE00601B

[38] Burgelman, M., Nollet, P., Degrave, S. "Modelling Polycrystalline Semiconductor Solar Cells", Thin Solid Films, 361–362, pp. 527–532, 2000. https://doi.org/10.1016/S0040-6090(99)00825-1

[39] Lenes, M., Morana, M., Brabec, C. J., Blom, P. W. M. "Recombination-Limited Photocurrents in Low Bandgap Polymer/Fullerene Solar Cells", Advanced Functional Materials, 19(7), pp. 1106–1111, 2009. https://doi.org/10.1002/adfm.200801514

[40] Sze, S. M., Ng, K. K. "Physics of Semiconductor Devices", Wiley, 2006. ISBN 9780470068328 https://doi.org/10.1002/0470068329

[41] Koster, L. J. A., Mihailetchi, V. D., Blom, P. W. M. "Bimolecular Recombination in Polymer/Fullerene Bulk Heterojunction Solar Cells", Applied Physics Letters, 88(5), 052104, 2006. https://doi.org/10.1063/1.2170424

[42] Deibel, C., Strobel, T., Dyakonov, V. "Role of the Charge Transfer State in Organic Donor–Acceptor Solar Cells", Advanced Materials, 22(37), pp. 4097–4111, 2010. https://doi.org/10.1002/adma.201000376

[43] Bartesaghi, D., Pérez, I. D. C., Kniepert, J., Roland, S., Turbiez, M., Neher, D., Koster, L. J. A. "Competition between Recombination and Extraction of Free Charges Determines the Fill Factor of Organic Solar Cells", Nature Communications, 6(1), 7083, 2015. https://doi.org/10.1038/ncomms8083

[44] Green, M. A. "Solar Cells: Operating Principles, Technology, and System Applications; Prentice-Hall series in solid state physical electronics", Prentice-Hall, 1982. ISBN 9780138222703

[45] Bisquert, J. "Theory of the Impedance of Electron Diffusion and Recombination in a Thin Layer", Journal of Physical Chemistry B, 106(2), pp. 325–333, 2002. https://doi.org/10.1021/jp011941g

[46] Street, R. A., Yang, Y., Thompson, B. C., McCulloch, I. "Capacitance Spectroscopy of Light Induced Trap States in Organic Solar Cells", The Journal of Physical Chemistry C, 120(39), pp. 22169–22178, 2016. https://doi.org/10.1021/acs.jpcc.6b06561

[47] Weiss, T. P., Nishiwaki, S., Bissig, B., Buecheler, S., Tiwari, A. N. "Voltage Dependent Admittance Spectroscopy for the Detection of near Interface Defect States for Thin Film Solar Cells", Physical Chemistry Chemical Physics, 19(45), pp. 30410–30417, 2017. https://doi.org/10.1039/C7CP05236G

[48] Jonscher, A. K. "The Universal Dielectric Response and Its Physical Significance", IEEE Transactions on Electrical Insulation, 27(3), pp. 407–423, 1992. https://doi.org/10.1109/14.142701

[49] Peumans, P., Yakimov, A., Forrest, S. R. "Small Molecular Weight Organic Thin-Film Photodetectors and Solar Cells", Journal of Applied Physics, 93(7), pp. 3693–3723, 2003. https://doi.org/10.1063/1.1534621

[50] Kyaw, A. K. K., Wang, D. H., Gupta, V., Leong, W. L., Ke, L., Bazan, G. C., Heeger, A. J. "Intensity Dependence of Current–Voltage Characteristics and Recombination in High-Efficiency Solution-Processed Small-Molecule Solar Cells", ACS Nano, 7(5), pp. 4569–4577, 2013. https://doi.org/10.1021/nn401267s

[51] Brabec, C. J., Gowrisanker, S., Halls, J. J. M., Laird, D., Jia, S., Williams, S. P. "Polymer–Fullerene Bulk-Heterojunction Solar Cells", Advanced Materials, 22(34), pp. 3839–3856, 2010. https://doi.org/10.1002/adma.200903697

[52] Würfel, P. "Physics of Solar Cells: From Principles to New Concepts", Wiley-VCH, 2005. ISBN 9783527618545 https://doi.org/10.1002/9783527618545

[53] Kirchartz, T., Gong, W., Hawks, S. A., Agostinelli, T., MacKenzie, R. C. I., Yang, Y., Nelson, J. "Sensitivity of the Mott–Schottky Analysis in Organic Solar Cells", The Journal of Physical Chemistry C, 116(14), pp. 7672–7680, 2012. https://doi.org/10.1021/jp300397f

[54] Shockley, W., Queisser, H. J. "Detailed Balance Limit of Efficiency of p-n Junction Solar Cells", Journal of Applied Physics, 32(3), pp. 510–519, 1961. https://doi.org/10.1063/1.1736034

[55] Varshni, Y. P. "Temperature Dependence of the Energy Gap in Semiconductors", Physica, 34(1), pp. 149–154, 1967. https://doi.org/10.1016/0031-8914(67)90062-6

[56] Garcia-Belmonte, G. "Temperature Dependence of Open-Circuit Voltage in Organic Solar Cells from Generation–Recombination Kinetic Balance", Solar Energy Materials and Solar Cells, 94(12), pp. 2166–2169, 2010. https://doi.org/10.1016/j.solmat.2010.07.006

[57] Blom, P. W. M., Mihailetchi, V. D., Koster, L. J. A., Markov, D. E. "Device Physics of Polymer: Fullerene Bulk Heterojunction Solar Cells", Advanced Materials, 19(12), pp. 1551–1566, 2007. https://doi.org/10.1002/adma.200601093